Journal of Materials Chemistry A

ROYAL SOCIETY OF CHEMISTRY

PAPER

View Article Online
View Journal | View Issue

Published on 03 January 2019. Downloaded by University of Science and Technology of China on 5/29/2020 3:30:25 AM.

Check for updates

Cite this: J. Mater. Chem. A, 2019, 7, 2291

Heterostructures of Ni–Co–Al layered double hydroxide assembled on V_4C_3 MXene for high-energy hybrid supercapacitors†

Xin Wang,[ab] Hui Li,[a] Han Li,[ab] Shuai Lin,*[a] Jin Bai,[ab] Jianming Dai,[a] Changhao Liang,[a] Xuebin Zhu,*[a] Yuping Sun[acd] and Shixue Dou[e]

Received 22nd November 2018
Accepted 3rd January 2019

DOI: 10.1039/c8ta11249e

rsc.li/materials-a

An energy storage system based on a battery-type electrode and a capacitive electrode as a hybrid supercapacitor offers a promising way to construct devices with advantages of both rechargeable batteries and carbon-based supercapacitors. NiCoAl-LDH nanosheets uniformly grow onto micron-scaled MXene sheets to form a NiCoAl-LDH/$V_4C_3T_x$ heterostructure with three-dimensional interconnected porous network microstructures by a hydrothermal method. NiCoAl-LDH/$V_4C_3T_x$ composite electrodes show an excellent specific capacity of 627 C g^{-1} at a current density of 1 A g^{-1} in 1 M KOH. Especially, the NiCoAl-LDH/$V_4C_3T_x$ electrodes exhibit a specific capacity of 300 C g^{-1} even at a high current density of 20 A g^{-1} in 1 M KOH, showing excellent rate performance. Hybrid supercapacitors, constructed with NiCoAl-LDH/$V_4C_3T_x$ as the battery-type electrode and activated carbon (AC) as the capacitive electrode, show superior energy densities of 71.7 and 45.0 W h kg^{-1} at power densities of 830 and 20 000 W kg^{-1} in 1 M KOH, respectively. The excellent capacity retention rate is 98% for the hybrid device after 10 000 cycles at 20 A g^{-1} in 1 M KOH. The NiCoAl-LDH/$V_4C_3T_x$ heterostructures can be used as promising electrode materials for low-cost hybrid supercapacitor devices.

1. Introduction

With the depletion of fossil fuels and increasing environmental pollution, the emergence of renewable energy (such as solar, wave and wind power) and electric vehicles is of great significance to sustainable development.[1,2] Therefore, the construction of energy storage devices, such as batteries (lead–acid, Ni–Cd, lithium ion, lithium–air/–sulfur,[3] sodium/aluminum ion batteries[4–7] and so on) and supercapacitors (electric double layer capacitors and pseudo-capacitors), is a key element to solve the energy crisis. Batteries have high energy density, but long charge–discharge time. On the other hand, supercapacitors can achieve fast charge–discharge to obtain higher power density, but the relatively low energy density limits their applications.[2]

To solve these problems, hybrid supercapacitor devices based on a battery-type electrode and a capacitive electrode are constructed, which show significantly higher energy density than conventional carbon-based supercapacitors, mainly due to the higher capacity of the battery-type electrode and the broader voltage window of the devices.[8–12] Moreover, the power density of hybrid devices is much higher than that of rechargeable batteries. Typically, a hybrid supercapacitor is constructed using a lithium electroactive material or a transition metal-based oxide/hydroxide and a carbon-based material, and electrochemical performance has been achieved in rGO@NiCoAl-LDHs//AC,[13] Ni–Co–Mn–OH/rGO//PPD/rGO,[8] Ni–Co phosphate//AC,[14] $NiMoO_4$//AC[15] hybrid/asymmetric supercapacitors and so on.

Layered double hydroxides (LDHs) have the potential to function as the battery-type electrode material for hybrid supercapacitors in alkaline electrolytes due to their high redox activity, high specific capacity, environmental friendliness and low cost.[16–18] In previous studies, LDHs have been widely reported as the typical "pseudocapacitive" electrode materials.[19–23] Recently, LDHs have been considered as battery-type materials because a pair of significant faradaic redox peaks with a relatively large potential separation is observed in the cyclic voltammetry (CV) curves, exhibiting the typical battery-type behaviour.[8,24–29] However, LDHs usually undergo irreversible phase transitions during charge and discharge, and the low electronic conductivity will lead to poor rate capability. To solve this problem, mixing of LDHs with conductive materials can

[a]Key Laboratory of Materials Physics, Institute of Solid State Physics, Hefei Institute of Physical Science, Chinese Academy of Sciences, Hefei 230031, People's Republic of China. E-mail: linshuai17@issp.ac.cn; xbzhu@issp.ac.cn

[b]University of Science and Technology of China, Hefei 230026, People's Republic of China

[c]High Magnetic Field Laboratory, Chinese Academy of Sciences, Hefei 230031, People's Republic of China

[d]Collaborative Innovation Center of Advanced Microstructures, Nanjing University, Nanjing 210093, People's Republic of China

[e]Institute for Superconducting and Electronic Materials, University of Wollongong, NSW 2500, Australia

† Electronic supplementary information (ESI) available. See DOI: 10.1039/c8ta11249e

Published on 03 January 2019. Downloaded by University of Science and Technology of China on 5/29/2020 3:30:25 AM.

improve the electrochemical performance.[20,21,30] For example, LDHs mixed with graphene nanosheets show improved electrochemical performance.

MXenes as a new type of two-dimensional (2D) materials, described as $M_{n+1}X_nT_x$, where T_x represents the adsorbed surface functional groups such as OH, O, and/or F, M is an early transition metal and X represents C and/or N, with $n = 1, 2, 3$, show chemical stability as well as high electrical conductivity.[31–37] Moreover, as a new type of electrode materials for supercapacitors, high specific capacitances have been observed in MXenes as well as excellent cycling stability.[34,38,39] For example, capacitance value can be as high as 900 F cm^{-3} at a scan rate of 2 mV s^{-1} for $Ti_3C_2T_x$.[34] Moreover, the superior capacitance retention rate is close to 100% after 10 000 cycles. Therefore, MXenes are considered as an ideal candidate to mix with LDHs to obviously improve the electrochemical performance in supercapacitors. In fact, MXenes have been used to mix with LDHs to improve the electrochemical performance recently.[20–22,40] For example, $Ti_3C_2T_x$/Ni–Co–Al-LDH heterostructures synthesized by a facile liquid-phase cofeeding and electrostatic attraction heteroassemble strategy exhibit a specific capacitance of 748.2 F g^{-1} and excellent rate performance.[21] To further improve the electrochemical performance, different MXenes, as a family with several types of structures including M_2XT_x such as V_2CT_x, Ti_2CT_x and Mo_2CT_x, $M_3X_2T_x$ such as $Ti_3C_2T_x$, $Hf_3C_2T_x$ and $Zr_3C_2T_x$, and the $M_4X_3T_x$ structure such as $Ti_4N_3T_x$, $Ta_4C_3T_x$ and $V_4C_3T_x$, are desirable to combine with different LDHs. V_4C_3 MXene ($V_4C_3T_x$), as a new type of MXene with a $M_4X_3T_x$ structure, has been successfully prepared recently.[41] From the viewpoint of the stability of MXenes, it is reported that the stability of MXenes is improved with increasing n,[37] which indicates that $V_4C_3T_x$ is relatively chemically stable and can endure processing with mixing of other electrode materials such as LDHs. On the other hand, V possesses rich valence states from +2 to +5, which is a bonus for electrochemical performance resulting in possible enhanced capacity.

Herein, NiCoAl-LDH/$V_4C_3T_x$ heterostructures with three-dimensional interconnected porous network microstructures were successfully prepared. High specific capacity and excellent rate capability are observed in NiCoAl-LDH/$V_4C_3T_x$ electrodes, showing a capacity of 300 C g^{-1} at a high current density of 20 A g^{-1} in 1 M KOH. Hybrid supercapacitors, constructed with NiCoAl-LDH/$V_4C_3T_x$ as the battery-type electrode and activated carbon (AC) as the capacitive electrode, show a maximum energy density of 71.7 W h kg^{-1} in 1 M KOH. Even at a high power density of 20 000 W kg^{-1}, the energy density can still remain at 45 W h kg^{-1} with a discharge time of 8.1 seconds. The results provide a type of hybrid supercapacitors based on NiCoAl-LDH/$V_4C_3T_x$ electrodes with excellent electrochemical performance.

2. Experimental section

2.1. Samples preparation

2.1.1. Synthesis of V_4C_3 MXene. Powders of V (Aladdin, 99.9%; −200 mesh), Al (Alfa Aesar, 99.9%; −325 mesh), and C (Sinopharm, 99.99%; −325 mesh) were mixed in an atomic ratio of 4 : 1.5 : 3. The mixture was pressed into pellets with a pressure of 1 GPa and then heated in a tube furnace under flowing argon. Heating processes are as follows: room temperature to 1000 °C at a heating rate of 9 °C min^{-1} and 5 °C min^{-1} from 1000 °C to 1500 °C. The samples were calcined at 1500 °C for 2 hours before furnace cooling to room temperature. After cooling to room temperature, the samples were crumbled by using a mortar and pestle in a glove box. The powders were submerged in a 40 wt% concentrated HF (Aladdin) solution for 96 h at 55 °C. After HF treatment, the resulting suspensions were washed several times using deionized water until the pH value of the supernatants was 6. The settled powders were then removed from vials using ethanol and dried in a vacuum oven at 60 °C for 12 h.

2.1.2. Synthesis of NiCoAl-LDH. The method for the synthesis of NiCoAl-LDH is as follows: $Ni(NO_3)_2 \cdot 6H_2O$ (0.55 g), $Co(NO_3)_2 \cdot 6H_2O$ (0.27 g), $Al(NO_3)_3 \cdot 9H_2O$ (0.35 g) and 0.75 g of urea were dissolved in deionized water (30 mL) at room temperature. The molar ratio of $Ni^{2+}/Co^{2+}/Al^{3+}$ was 2 : 1 : 1. The homogeneous solution after stirring was then transferred into a Teflon-lined stainless steel autoclave (100 mL in capacity). After that, the autoclave was sealed and heated at 120 °C for 10 h. After cooling to room temperature, the precipitates were centrifuged out and washed several times with deionized water (30 mL), and then dried at 70 °C for 24 h.

2.1.3. Synthesis of the NiCoAl-LDH/$V_4C_3T_x$ composite. The method for the synthesis of NiCoAl-LDH/$V_4C_3T_x$ is as follows: $Ni(NO_3)_2 \cdot 6H_2O$, $Co(NO_3)_2 \cdot 6H_2O$, $Al(NO_3)_3 \cdot 9H_2O$ and urea were dissolved in 30 mL deionized water (the usage was the same as that aforementioned); 0.05 g of $C_6H_8O_7 \cdot H_2O$ and 0.1 g of V_4C_3 MXene were further added to the solution under constant stirring. The homogeneous solution was then transferred into a Teflon-lined stainless steel autoclave (100 mL in capacity). After that, the autoclave was sealed and heated at 120 °C for 10 h. After cooling to room temperature, the precipitates were collected by means of centrifugation and washed several times with deionized water. Then, they were dried at 70 °C for 24 h. The weight percentage of V_4C_3 MXene in the NiCoAl-LDH/$V_4C_3T_x$ composite is about 25% and the mass ratio of NiCoAl-LDH to $V_4C_3T_x$ is about 3 : 1. It should be pointed out here that citric acid ($C_6H_8O_7 \cdot H_2O$) acting as a surfactant was added into the solution, leading to the easy growth of NiCoAl-LDH nanosheets onto the micron-scaled $V_4C_3T_x$ during the hydrothermal synthesis.

2.2. Materials characterization

Microstructure characterizations were achieved by recording X-ray diffraction (XRD) patterns (Philips X'pert PRO X-ray diffractometer with Cu K_α radiation, $\lambda = 0.15406$ nm), and by performing field emission scanning electron microscopy (FE-SEM, Quanta 200 FEG) and energy-dispersive X-ray spectroscopy (EDX, Oxford EDX, with INCA software), transmission electron microscopy (TEM, JEM-2100) with configured EDX, and X-ray photoelectron spectroscopy (XPS, Thermo ESCALAB 250Xi equipped with a monochromatic Al K_α source of 1486.6 eV).

 This journal is © The Royal Society of Chemistry 2019

Published on 03 January 2019. Downloaded by University of Science and Technology of China on 5/29/2020 3:30:25 AM.

2.3. Electrochemical measurement and evaluation

For the electrochemical tests of electrode materials (NiCoAl-LDH, $V_4C_3T_x$ and NiCoAl-LDH/$V_4C_3T_x$), the working electrodes in a three-electrode configuration were fabricated as follows: a mixture of active material, acetylene black, and polyvinylidene fluoride (PVDF) at a weight ratio of 80 : 10 : 10 was uniformly cast on nickel foams. The area of the working electrodes is 1 cm^2, and the mass loading of electrodes is about 2 mg. Electrodes were dried at 90 °C for 12 hours. Platinum and Ag/AgCl in 3 M KCl were the counter electrode and the reference electrode, respectively. Cyclic voltammetry (CV) was conducted in a voltage window between −0.1 and 0.5 V, and galvanostatic charge–discharge (GCD) was measured between −0.1 and 0.45 V (*vs.* Ag/AgCl). Electrochemical impedance spectroscopy (EIS) was performed with open circuit voltage in the frequency range of 100 kHz to 0.01 Hz combined with a 5.0 mV disturbing signal. The specific capacity Q of the electrodes is calculated as:

$$Q = I\Delta t/m \quad (1)$$

where I, Δt, and m represent the constant discharge current (A), discharge time (s) and mass of active materials (g), respectively.

The NiCoAl-LDH/$V_4C_3T_x$ composite and activated carbon (AC) are assembled into a two-electrode Swagelok-type cell to construct hybrid supercapacitors. In order to achieve the best electrochemical performance of the NiCoAl-LDH/$V_4C_3T_x$//AC hybrid device, the charge balance is determined as $q^+ = q^-$.

$$q = \int jm\mathrm{d}V/v \quad (2)$$

where j is the constant current density (A g^{-1}), m (g) is the mass of the active material, V is the potential window, v is the scan rate (V s^{-1}), and $\int j\mathrm{d}V$ is the integral area of the cyclic voltammogram. To achieve $q^+ = q^-$, the mass of the active material on the electrode definitely is:

$$m_+ : m_- = \left(\int j\mathrm{d}V/v\right)_- : \left(\int j\mathrm{d}V/v\right)_+ \quad (3)$$

Therefore, it was found that the positive and negative mass ratio of the NiCoAl-LDH/$V_4C_3T_x$//AC hybrid device is about 1 : 3. Cyclic voltammetry (CV) was performed in a voltage window between 0 and 1.60 V, and the galvanostatic charge–discharge (CD) was measured between 0 and 1.60 V. The energy density and power density of hybrid devices were calculated according to the following equations:

$$E = j\int V\mathrm{d}t/3.6 \quad (4)$$

$$P = E/\Delta t \quad (5)$$

where j is the constant current density (A g^{-1}), V is the voltage (V) and the time (Δt) is in seconds, E (W h kg^{-1}) is the energy density, and P (W kg^{-1}) is the power density. All electrochemical measurements were carried out on a CHI 660E electrochemical work station in KOH electrolyte.

3. Results and discussion

The synthetic process of the NiCoAl-LDH/$V_4C_3T_x$ composite with three-dimensional (3D) interconnected porous network microstructures is illustrated in Scheme 1. Firstly, V_4AlC_3 powders were etched in hydrofluoric acid (HF) to obtain V_4C_3 MXene. Functional groups such as OH, O, and/or F are introduced on the MXene surfaces, which facilitate nucleation of the NiCoAl-LDH nanosheets and firmly anchor them onto the V_4C_3 MXene sheets. Then, the V_4C_3 MXene sheets and $C_6H_8O_7\cdot H_2O$ were dispersed in a solution containing Ni^{2+}, Co^{2+}, Al^{3+} and urea to synthesize three-dimensional interconnected porous NiCoAl-LDH/$V_4C_3T_x$ composites.

As shown by the FE-SEM images in Fig. 1a–c and the TEM image in Fig. 1d for the prepared NiCoAl-LDH/$V_4C_3T_x$, it is clearly observed that NiCoAl-LDH nanosheets can uniformly grow onto the micron-scaled MXene sheets with three-dimensional interconnected porous network microstructures. The presence of V, C, F, Ni, Co, Al and O elements in the NiCoAl-LDH/$V_4C_3T_x$ composite is confirmed from the EDS spectra as shown in Fig. 1f. The uniform distribution of V, C, F, Ni, Co, Al and O elements is visualized by elemental mapping analysis as presented in Fig. 1g. As shown in Fig. 1e of the XRD results for the NiCoAl-LDH/$V_4C_3T_x$ heterostructures, the peaks located at 2θ of 11.36°, 23.25°, 34.53°, 37.55 and 61.40° can be respectively ascribed to the (003), (006), (012), (015) and (110) peaks of NiCoAl-LDH, and the peak located at 2θ of 5.43° can be indexed to the (002) peak of $V_4C_3T_x$ MXene. To further confirm the NiCoAl-LDH phase, high-resolution TEM (HRTEM) from the selected areas (Fig. S1†) gives an interlayer spacing of about 0.22 nm (1.12/5), and FFT reveals a hexagonal structure, which agree well with the *d*-spacing of the (006) plane and the crystal structure of the NiCoAl-LDH phase, further confirming the successful synthesis of the NiCoAl-LDH phase. The corresponding XRD patterns, FE-SEM images, TEM images, elemental mapping images and EDS spectra of Ni–Co–Al-LDH are shown in Fig. S2,† from which one can clearly see that well-crystallized Ni–Co–Al-LDH nanosheets with uniform elemental distribution have been successfully obtained. On the other hand, the corresponding XRD patterns, FE-SEM images, TEM images, elemental mapping images and EDS spectra of the $V_4C_3T_x$ MXene are shown in Fig. S3,† from which it is obviously observed that $V_4C_3T_x$ with organ-like morphology can be successfully obtained. The above results confirm that well-crystallized NiCoAl-LDH nanosheets can uniformly grow onto micron-scaled $V_4C_3T_x$ sheets.

X-ray photoelectron spectroscopy (XPS) was used to determine the elemental valences in the derived NiCoAl-LDH/$V_4C_3T_x$ heterostructures. All the XPS peaks were calibrated with C 1s. As shown in Fig. 2a, the coexistence of V, C, Ni, Co, Al and O elements is further confirmed. The corresponding Ni 2p spectrum (Fig. S4a†), Co 2p spectrum (Fig. S4b†) and Al 2p peak (Fig. S4c†) spectrum confirm that the valences are Ni^{2+}, Co^{2+} and Al^{3+} in the NiCoAl-LDH/$V_4C_3T_x$ composite. High-resolution

Published on 03 January 2019. Downloaded by University of Science and Technology of China on 5/29/2020 3:30:25 AM.

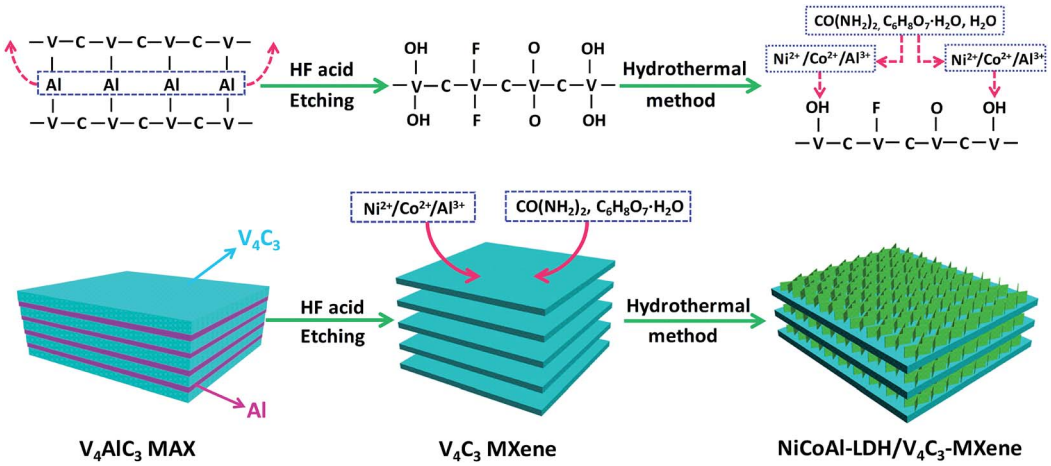

Scheme 1 Schematic diagram of the synthetic process of the NiCoAl-LDH/$V_4C_3T_x$ composite.

XPS analysis is performed and the results are shown in Fig. 2b–g. As shown in Fig. 2b and c, the Ni $2p_{3/2}$ and Ni $2p_{1/2}$ peaks in NiCoAl-LDH/$V_4C_3T_x$ are significantly offset as compared to the pure NiCoAl-LDH by 0.33 eV and 0.25 eV, respectively. Fig. 2d,e and f give comparisons between Co $2p_{3/2}$, Co $2p_{1/2}$ and Al 2p respectively, from which it is seen that the binding energy is shifted by about 0.37, 0.51 and 0.33 eV as compared to the pure NiCoAl-LDH, respectively. The binding energy of O 1s also shifts by about 0.23 eV as shown in Fig. 2g. The significant changes in the binding energies of the elements are similar to the previous report,[40] suggesting the chemical bonding between NiCoAl-LDH and V_4C_3 MXene in the NiCoAl-LDH/$V_4C_3T_x$ heterostructures.

Cyclic voltammetry (CV) measurements were carried out on the NiCoAl-LDH, $V_4C_3T_x$ and NiCoAl-LDH/$V_4C_3T_x$ electrodes at a scan rate of 2 mV s^{-1} and the results are shown in Fig. 3a. A pair of distinctly faradaic redox peaks with a relatively large potential separation is visible for all three samples, exhibiting the typical battery-type behaviour.[26–28] Furthermore, with increase in the scan rate, the anodic and cathodic peaks respectively shift in the positive and negative directions due to the polarization effects (Fig. S5a–c†). At a scan rate of 10 mV s^{-1} and higher rates (Fig. S5†), the CV area of the NiCoAl-LDH/

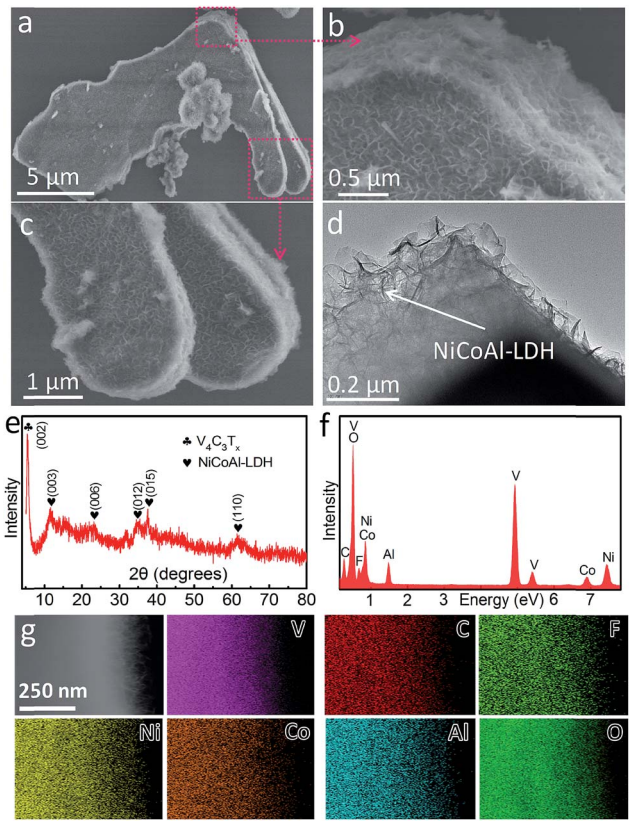

Fig. 1 Characterization of NiCoAl-LDH/$V_4C_3T_x$ heterostructures. (a–c) FE-SEM images, (d) TEM image, (e) XRD pattern, (f) EDS spectra and (g) TEM image, and corresponding elemental mapping images of Ni, Co, Al, O, V, C and F elements of NiCoAl-LDH/$V_4C_3T_x$ heterostructures.

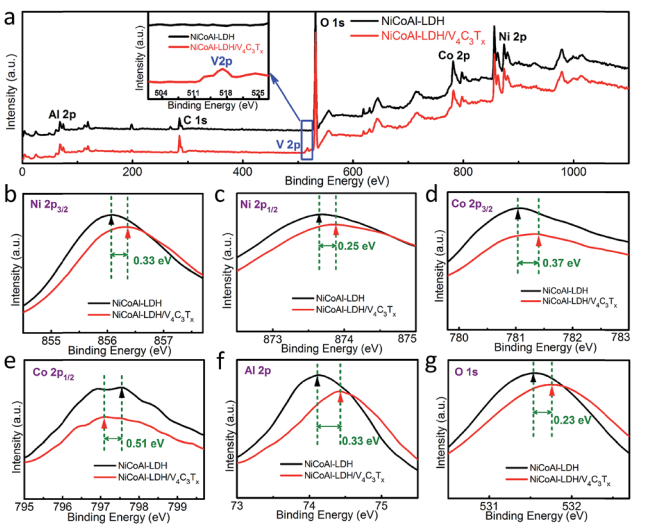

Fig. 2 (a) XPS survey scans of NiCoAl-LDH and NiCoAl-LDH/$V_4C_3T_x$, with the inset showing an enlargement of the XPS spectra from 501 to 527 eV. (b) Ni $2p_{3/2}$, (c) Ni $2p_{1/2}$, (d) Co $2p_{3/2}$, (e) Co $2p_{1/2}$, (f) Al 2p and (g) O 1s XPS spectra of NiCoAl-LDH/$V_4C_3T_x$ heterostructures.

This journal is © The Royal Society of Chemistry 2019

Published on 03 January 2019. Downloaded by University of Science and Technology of China on 5/29/2020 3:30:25 AM.

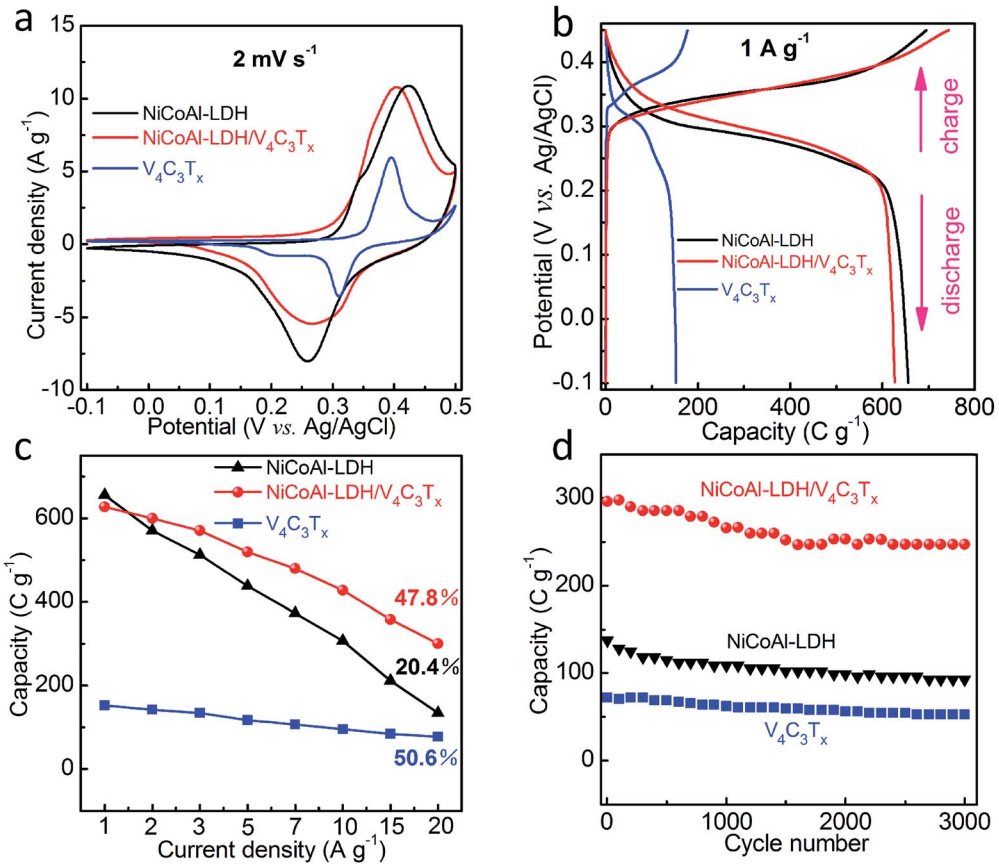

Fig. 3 (a) Cyclic voltammetry (CV) measurements at a scan rate of 2 mV s^{-1}, (b) galvanostatic charge–discharge curves at 1 A g^{-1}. (c) Gravimetric specific capacity of the electrodes plotted as a function of current densities and (d) cycling performance at 20 A g^{-1} of NiCoAl-LDH, $V_4C_3T_x$ and NiCoAl-LDH/$V_4C_3T_x$ electrodes in 1 M KOH.

$V_4C_3T_x$ heterostructures becomes the largest, suggesting the highest specific capacity. Galvanostatic charge–discharge tests of the electrodes were carried out at various current densities (Fig. S6a–c†) and the obvious charge–discharge platforms also demonstrate the battery-type behaviour of the electrodes, which is similar to the CV results. Fig. 3b shows the galvanostatic charge–discharge curves of the samples at a current density of 1 A g^{-1}; one can see that both NiCoAl-LDH and NiCoAl-LDH/$V_4C_3T_x$ electrodes can deliver high capacities of 656 C g^{-1} and 627 C g^{-1} at 1 A g^{-1}, respectively, which suggests that the addition of the conductive $V_4C_3T_x$ does not lead to obvious decrease in the capacity of the NiCoAl-LDH. In addition, CV and GCD tests were also carried out on the NiCoAl-LDH/$V_4C_3T_x$ heterostructure electrodes in 1, 3 and 6 M KOH (Fig. S7†). With increase in the KOH concentration, the redox peak shifts to a lower potential and the potential of the charge–discharge platform is lowered at higher concentrations as shown in Fig. S7a and b.† Besides, the higher the concentration of KOH is, the longer the charge–discharge time. As shown in Fig. S7c,† a specific capacitance of 1445 F g^{-1} at 2 A g^{-1} and 1094 F g^{-1} at 10 A g^{-1} is obtained in 6 M KOH (as shown in Table S1 and Fig. S7d–f†). On the other hand, with increase in the KOH concentration, the potential window is lowered, which is similar to the previous report.[42] As a result, 1 M KOH electrolyte was used in the following measurements.

With increase in the scan rate, the kinetics will play a very important role in the determination of the capacity. As shown in Fig. 3c (Fig. S6,† corresponding to the galvanostatic charge–discharge curves), the NiCoAl-LDH/$V_4C_3T_x$ electrodes show superior electrochemical performance with increase in the scan rate. The NiCoAl-LDH electrodes exhibit a discharge capacity of 656 C g^{-1} at 1 A g^{-1}. The discharge capacity quickly drops to 134 C g^{-1} at 20 A g^{-1}, which is only, however, 20.4% of the capacity at 1 A g^{-1}. The $V_4C_3T_x$ electrodes show excellent rate performance and the capacity is 152 C g^{-1} at 1 A g^{-1} and it is 77 C g^{-1} at 20 A g^{-1} (Table S2†). Interestingly, the NiCoAl-LDH/$V_4C_3T_x$ heterostructures exhibit not only a high discharge capacity but also excellent rate performance. Especially, the NiCoAl-LDH/$V_4C_3T_x$ electrodes exhibit a specific capacity of 300 C g^{-1} even at a high current density of 20 A g^{-1}. Electrochemical properties of the NiCoAl-LDH physically mixed $V_4C_3T_x$ electrodes (NiCoAl-LDH + V_4C_3-MXene, 75 wt% NiCoAl-LDH) have also been measured for comparison. As shown in Fig. S8a,† the NiCoAl-LDH/$V_4C_3T_x$ heterostructure shows a higher capacity (627 C g^{-1}) than the NiCoAl-LDH mixed $V_4C_3T_x$ (481 C g^{-1}) at a current density of 1 A g^{-1} and the capacity of NiCoAl-LDH/$V_4C_3T_x$ can still remain at 300 C g^{-1} at 20 A g^{-1} (Table S2, Fig. S8b and c†), confirming the enhanced performance for the heterostructure. Fig. 3d shows the cycling stability of the NiCoAl-LDH, the $V_4C_3T_x$ and the NiCoAl-LDH/$V_4C_3T_x$ electrodes at a high current

Published on 03 January 2019. Downloaded by University of Science and Technology of China on 5/29/2020 3:30:25 AM.

density of 20 A g^{-1} for 3000 cycles. After 3000 cycles, the specific capacities of NiCoAl-LDH and $V_4C_3T_x$ electrodes are reduced from 138 C g^{-1} and 72 C g^{-1} to 93 C g^{-1} and 52 C g^{-1}, respectively, while the NiCoAl-LDH/$V_4C_3T_x$ electrodes can still maintain a specific capacity of 248 C g^{-1}, showing excellent cycling stability.

To further evaluate the electrochemical behavior of the samples, EIS spectra were measured as shown in Fig. S9.† The Nyquist plots of NiCoAl-LDH, $V_4C_3T_x$ and NiCoAl-LDH/$V_4C_3T_x$ are shown in Fig. S9a.† At high frequency, the intersection on the real axis gives the internal resistances of the electrode (R_s). As for the $V_4C_3T_x$ electrode, the juncture on the real axis is the smallest (Fig. S9a†), exhibiting the smallest charge-transfer resistance among the three electrodes.[21] In the low-frequency region the NiCoAl-LDH/$V_4C_3T_x$ electrode shows a larger slope than NiCoAl-LDH, indicating enhanced ion-transfer ability compared to that of NiCoAl-LDH. In addition, a capacitor frequency response can be obtained at an impedance phase angle of −45°, where the resistance and reactance reach an equal value as shown in Fig. S9b.† It is noted that the knee frequency of the NiCoAl-LDH/$V_4C_3T_x$ electrode is estimated to be about 56 Hz, which is higher than that of the NiCoAl-LDH (10 Hz) nanosheets and suggests the excellent rate performance of the NiCoAl-LDH/$V_4C_3T_x$ electrode.[43,44] The enhancement may be attributed to the introduction of high electrical conductivity and charge transport efficiency for V_4C_3 MXene.[21]

To demonstrate the potential applications of the NiCoAl-LDH/$V_4C_3T_x$ heterostructures, hybrid supercapacitors were constructed as sketched in Fig. 4a, in which NiCoAl-LDH/$V_4C_3T_x$ is used as the battery-type electrode (positive electrode), activated carbon (AC) is the capacitive electrode (negative electrode), cellulose papers are used as separators and the electrolyte is 1 M KOH solution. Besides, the AC electrodes were also measured and the detailed results confirm a voltage window between −1 and 0 V (Fig. S10 and Table S3†) and the capacitance retention rate is 99.98% for the AC electrode after 6000 cycles at 15 A g^{-1} (Fig. S10d†). The possible operating voltage of the hybrid devices is studied by cyclic voltammetry (Fig. 4b), from which it is seen that the most suitable voltage window is 0–1.6 V. Further increasing the maximum operating voltage to 1.8 V will lead to a sharp increase in current density due to the electrolyte decomposition/water splitting.[8] Charge–discharge tests of the NiCoAl-LDH/$V_4C_3T_x$//AC hybrid devices were carried out at various current densities within the potential window between 0 and 1.60 V, and the corresponding results are shown in Fig. 4c. The triangular shapes for the charge and discharge curves with a very small charge and discharge platform suggest that both the positive and negative electrodes contribute to the specific capacity. Fig. 4d shows the rate capability of the NiCoAl-LDH/$V_4C_3T_x$//AC device. It is seen that the hybrid device shows a high specific capacitance of 194 F g^{-1} at a current density of 1 A g^{-1}, and the capacitance still remains at 102 F g^{-1} at a higher current density of 20 A g^{-1} (Table S4†), indicating the excellent rate capability of the NiCoAl-LDH/$V_4C_3T_x$//AC hybrid device. Fig. 4e shows the cycling stability of the NiCoAl-LDH/$V_4C_3T_x$//AC hybrid device at a high current density of 20 A g^{-1} for 10 000 cycles in a potential window of 0–1.6 V. It is observed that the capacity retention rate is 98% for the NiCoAl-LDH/$V_4C_3T_x$//AC hybrid device after 10 000 cycles, which is comparable with the previously reported advanced hybrid/asymmetric

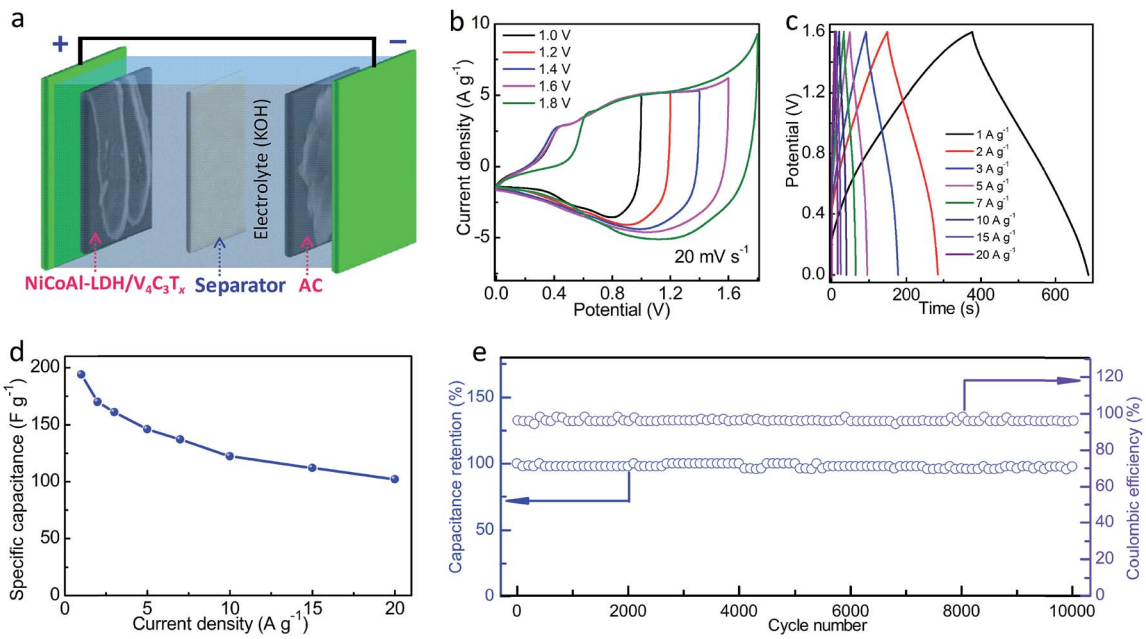

Fig. 4 Electrochemical testing of hybrid devices in 1 M KOH. (a) Schematic illustration of the NiCoAl-LDH/$V_4C_3T_x$//AC hybrid supercapacitor device. (b) CV curves at scan rate of 20 mV s^{-1} under different operating voltage windows. (c) Galvanostatic charge–discharge curves of the NiCoAl-LDH/$V_4C_3T_x$//AC hybrid devices at different current densities from 1 to 20 A g^{-1}. (d) Specific capacitances of the NiCoAl-LDH/$V_4C_3T_x$//AC device at different discharge current densities. (e) Cycling performance of the NiCoAl-LDH/$V_4C_3T_x$//AC hybrid devices at 20 A g^{-1} within the potential window between 0 and 1.60 V.

 This journal is © The Royal Society of Chemistry 2019

Published on 03 January 2019. Downloaded by University of Science and Technology of China on 5/29/2020 3:30:25 AM.

supercapacitors (Table S5†).[8,14,15,45–57] The coulombic efficiency of the NiCoAl-LDH/$V_4C_3T_x$//AC hybrid device is about 96% during the cycling test after initial activation (Fig. 4e), which also suggests the high cycling stability. Fig. 5a shows the cyclic voltammetry (CV) curves of the NiCoAl-LDH/$V_4C_3T_x$//AC hybrid devices at the scan rates of 5, 10, 20, 30, 50 and 100 mV s^{-1}. One can clearly see that the shape of the CV curves is efficiently maintained and the redox peak is slightly offset with increase in the current density, indicating the high rate capability of the hybrid devices. As for the enhanced cycling stability for the hybrid device as compared with the NiCoAl-LDH/$V_4C_3T_x$ electrode measured with the three electrode configuration, it is seen that the former one exhibits enhanced capacitive electrochemical performance, whereas the electrochemical properties show typical battery-like behaviour as confirmed from the CV and charge–discharge results for the latter one. The capacitive behavior will lead to enhanced cycling stability.[58] The capacitive behavior can be attributed to the configuration of the hybrid device with AC as the negative electrode, which is further confirmed from the kinetic analysis.

CV tests at various scan rates from 5 to 100 mV s^{-1} are conducted to analyze the kinetics of the NiCoAl-LDH/$V_4C_3T_x$//AC hybrid supercapacitors. The i measured can be interpreted as the sum of the current related to the slow diffusion-controlled process (i_{diff}) and surface capacitance-dominated process (i_{cap}), which can be described by eqn (6) and (7):[59–61]

$$i = i_{cap} + i_{diff} = av^b \quad (6)$$

$$\log i = \log a + b \log v \quad (7)$$

It is known that in the diffusion-controlled process b approaches 0.5, while for a surface capacitance-dominated process b is close to 1.0.[59–61] The range of b value from 0.5 to 1.0 indicates a "transition" area between the capacitive materials and the battery-type materials. As shown in Fig. 5b for the NiCoAl-LDH/$V_4C_3T_x$//AC hybrid device, the resulting b-values fall in the range of 0.69–1.0, suggesting a coupled diffusion-controlled and capacitive process for storage in the NiCoAl-LDH/$V_4C_3T_x$//AC hybrid device.

Further quantification of the capacitive contribution to the total current is analyzed using eqn (8) and (9).[59–61]

$$i(V) = i_{cap} + i_{diff} = k_1 v + k_2 v^{1/2} \quad (8)$$

For analytical purposes, eqn (3) can be written as

$$i(V)/v^{1/2} = k_1 v^{1/2} + k_2 \quad (9)$$

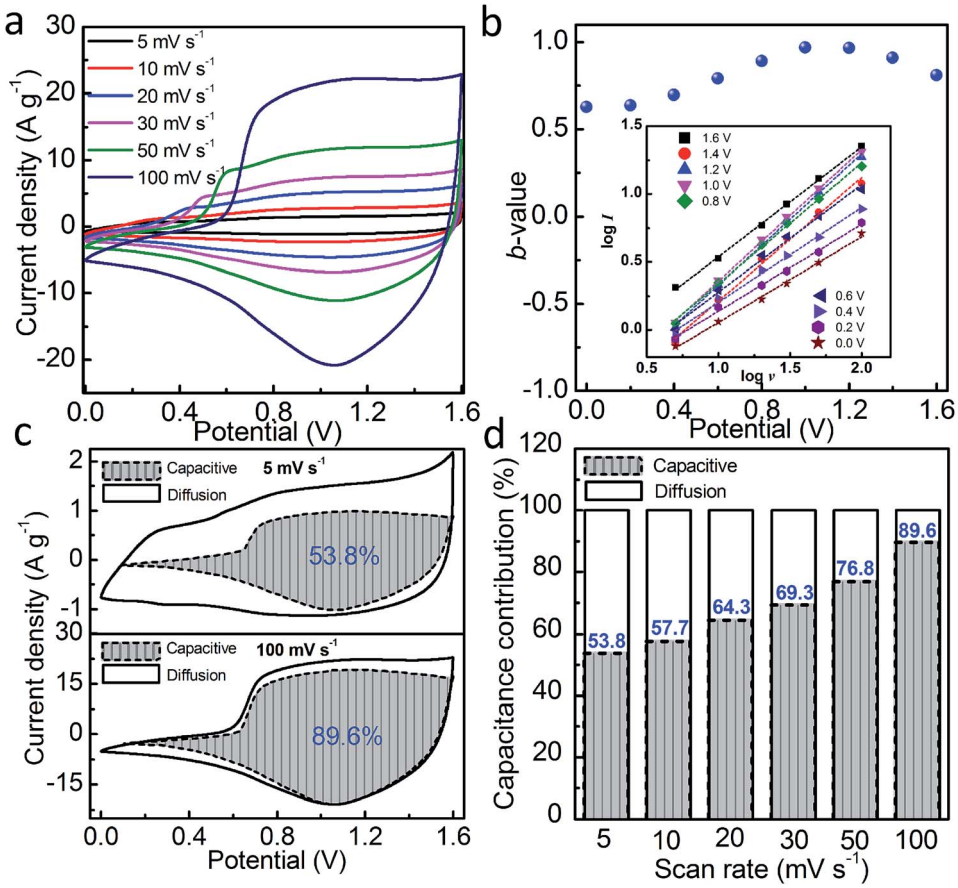

Fig. 5 (a) Comparison of CV curves of the NiCoAl-LDH/$V_4C_3T_x$//AC hybrid supercapacitor at different scan rates. (b) b-Values for the hybrid supercapacitor. Inset: plot of log I *versus* log v (see eqn (6) and (7) in the text). (c) CV partition analysis showing capacitive contribution to total current at select scan rates. (d) Normalized contribution ratio of capacitive capacities at different scan rates.

Published on 03 January 2019. Downloaded by University of Science and Technology of China on 5/29/2020 3:30:25 AM.

As shown in Fig. 5c and d, the capacitive contribution to the total current increases from 53.8% at 5 mV s^{-1} to 89.6% at 100 mV s^{-1}. The capacitive contribution to the NiCoAl-LDH/$V_4C_3T_x$//AC hybrid device at 10, 20, 30, and 50 mV s^{-1} is also calculated (Fig. S11†). The results show that, at scan rates below 5 mV s^{-1}, the contribution of the diffusion-limited process to the total capacity is noticeable. At scan rates of 100 mV s^{-1} and higher, the response is not diffusion-controlled but the surface capacitive effects are, which is beneficial to achieve high power density at high current densities. The high b values and the broad peaks in the CV curves strongly suggest that surface capacitive behavior is the major operative mechanism in the NiCoAl-LDH/$V_4C_3T_x$//AC hybrid device, which indicates the ultra-fast energy storage ability.

The values of energy density and power density of the NiCoAl-LDH/$V_4C_3T_x$//AC hybrid device are calculated from the galvanostatic discharge curves. As presented in Fig. 6b, the energy density dependence on power density is plotted and it is seen that the NiCoAl-LDH/$V_4C_3T_x$//AC hybrid device shows a high energy density of 71.7 W h kg^{-1} at a power density of 830 W kg^{-1}, and the energy density still remains at 45.0 W h kg^{-1} at a higher power density of 20 000 W kg^{-1} with a discharge time of 8.1 seconds, indicating that the NiCoAl-LDH/$V_4C_3T_x$//AC hybrid device has ultra-fast energy storage ability. The detailed data (Table S6†) suggest that the NiCoAl-LDH/$V_4C_3T_x$//AC hybrid device can serve as an excellent energy storage device. In order to meet the needs of practical applications, multiple NiCoAl-LDH/$V_4C_3T_x$//AC hybrid devices need to be connected in series to achieve specific voltage values, energy and power density (Fig. 6a). The voltage window of a single hybrid device is 1.6 V, and the charge–discharge voltage window of the two devices in series can be increased to 3.2 V (Fig. 6c). In addition, as shown in Fig. 6d, the device constructed from the two NiCoAl-LDH/$V_4C_3T_x$//AC hybrid devices connected in series can light up blue, green, yellow and red light-emitting diodes (LEDs), demonstrating its potential applications in energy storage.

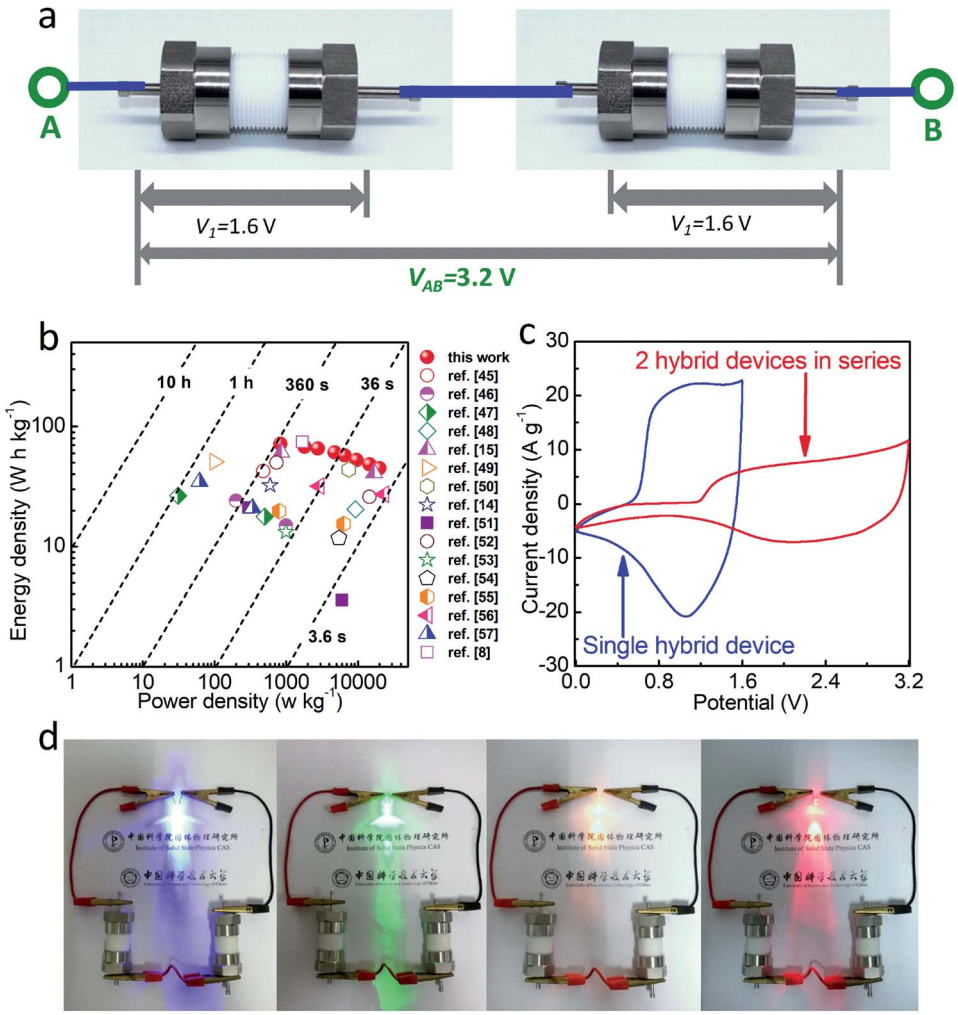

Fig. 6 (a) Equivalent circuit schematic of the device of two NiCoAl-LDH/$V_4C_3T_x$//AC hybrid devices connected in series. (b) Ragone plot of power and energy densities of NiCoAl-LDH/$V_4C_3T_x$//AC hybrid devices compared to the previously reported advanced hybrid/asymmetric supercapacitors. (c) CV curves of the single hybrid device and the two hybrid devices connected in series. The single device can sustain 1.6 V, such that the series connection of two capacitors can supply output potential up to 3.2 V. However, the total current decreases because of the overlying cell resistance from two hybrid devices. (d) Photographs of the two hybrid devices connected in series which can drive blue, green, yellow and red light-emitting diodes (LEDs).

 This journal is © The Royal Society of Chemistry 2019

Published on 03 January 2019. Downloaded by University of Science and Technology of China on 5/29/2020 3:30:25 AM.

4. Conclusions

In summary, NiCoAl-LDH/$V_4C_3T_x$ heterostructures with three-dimensional interconnected porous network microstructures were successfully prepared by a hydrothermal method, showing battery-type electrode behavior with a specific capacity of 627 C g^{-1} at a current density of 1 A g^{-1} in 1 M KOH. Especially, the NiCoAl-LDH/$V_4C_3T_x$ heterostructures show excellent rate performance, exhibiting a specific capacity of 300 C g^{-1} at a high current density of 20 A g^{-1} in 1 M KOH. Furthermore, hybrid supercapacitors, constructed using NiCoAl-LDH/$V_4C_3T_x$ as the battery-type electrode and activated carbon (AC) as the capacitive electrode, show a maximum energy density of 71.7 W h kg^{-1} in 1 M KOH. Even at a high power density of 20 000 W kg^{-1}, the energy density can still remain at 45 W h kg^{-1} with a discharge time of 8.1 seconds, indicating that the NiCoAl-LDH/$V_4C_3T_x$//AC hybrid devices have ultra-fast energy storage ability. The NiCoAl-LDH/$V_4C_3T_x$ heterostructures can be used as a promising electrode material for hybrid supercapacitors.

Conflicts of interest

There are no conflicts to declare.

Acknowledgements

This work was supported by the National Key R&D Program of China (Grant No. 2016YFA0401801, 2014CB931704), Natural Science Foundation of Anhui Province (Grant 1608085QE107), and Key Research Program of Frontier Sciences, CAS (QYZDB-SSW-SLH015). Additionally, this work was also supported by the Youth Innovation Promotion Association of CAS (Grant 2014283). The authors thank Dr Tania Silver at University of Wollongong, Australia, for improvement of the English.

Notes and references

1 B. Dunn, H. Kamath and J. M. Tarascon, *Science*, 2011, **334**, 928–935.
2 W. Zuo, R. Li, C. Zhou, Y. Li, J. Xia and J. Liu, *Adv. Sci.*, 2017, **4**, 1600539.
3 P. G. Bruce, S. A. Freunberger, L. J. Hardwick and J. M. Tarascon, *Nat. Mater.*, 2011, **11**, 19–29.
4 S. Y. Hong, Y. Kim, Y. Park, A. Choi, N. S. Choi and K. T. Lee, *Energy Environ. Sci.*, 2013, **6**, 2067–2081.
5 N. Jayaprakash, S. K. Das and L. A. Archer, *Chem. Commun.*, 2011, **47**, 12610.
6 C. D. Wessells, S. V. Peddada, R. A. Huggins and Y. Cui, *Nano Lett.*, 2011, **11**, 5421–5425.
7 Q. Zhao, J. Wang, Y. Lu, Y. Li, G. Liang and J. Chen, *Angew. Chem., Int. Ed.*, 2016, **55**, 12528–12532.
8 B. T. Zhao, L. Zhang, Q. B. Zhang, D. C. Chen, Y. Cheng, X. Deng, Y. Chen, R. Murphy, X. H. Xiong, B. Song, C. P. Wong, M. S. Wang and M. L. Liu, *Adv. Energy Mater.*, 2018, **8**, 1702247.
9 S. Dai, B. Zhao, C. Qu, D. C. Chen, D. Dang, B. Song, B. M. Deglee, J. W. Fu, C. G. Hu, C. P. Wong and M. L. Liu, *Nano Energy*, 2017, **33**, 522–531.
10 J. B. Cook, H. S. Kim, T. C. Lin, C. H. Lai, B. Dunn and S. H. Tolbert, *Adv. Energy Mater.*, 2017, **7**, 1601283.
11 J. H. Won, H. M. Jeong and J. K. Kang, *Adv. Energy Mater.*, 2017, **7**, 1601355.
12 H. W. Wang, Y. Zhang, H. X. Ang, Y. Q. Zhang, H. T. Tan, Y. F. Zhang, Y. Y. Guo, J. B. Franklin, X. L. Wu, M. Srinivasan, H. J. Fan and Q. Y. Yan, *Adv. Funct. Mater.*, 2016, **26**, 3082–3093.
13 D. X. Guo, X. M. Song, L. C. Tan, H. Y. Ma, W. F. Sun, H. J. Pang, L. L. Zhang and X. M. Wang, *Chem. Eng. J.*, 2019, **356**, 955–963.
14 B. Li, P. Gu, Y. Feng, G. Zhang, K. Huang, H. Xue and H. Pang, *Adv. Funct. Mater.*, 2017, **27**, 1605748.
15 S. J. Peng, L. L. Li, H. B. Wu, S. Madhavi and X. W. Lou, *Adv. Energy Mater.*, 2015, **5**, 1401172.
16 M. Shao, R. Zhang, Z. Li, M. Wei, D. G. Evans and X. Duan, *Chem. Commun.*, 2015, **51**, 15880–15893.
17 J. Cheng, J. Zhang and F. Liu, *RSC Adv.*, 2014, **4**, 38893–38917.
18 R. Ma, J. Liang, X. Liu and T. Sasaki, *J. Am. Chem. Soc.*, 2012, **134**, 19915–19921.
19 X. Wang, Y. Y. Lin, Y. Su, B. Zhang, C. J. Li, H. Wang and L. J. Wang, *Electrochim. Acta*, 2017, **225**, 263–271.
20 Y. Wang, H. Dou, J. Wang, B. Ding, Y. L. Xu, Z. Chang and X. D. Hao, *J. Power Sources*, 2016, **327**, 221–228.
21 R. Z. Zhao, M. Q. Wang, D. Y. Zhao, H. Li, C. X. Wang and L. W. Yin, *ACS Energy Lett.*, 2018, **3**, 132–140.
22 H. Li, F. Musharavati, E. Zalenezhad, X. Chen, K. N. Hui and K. S. Hui, *Electrochim. Acta*, 2018, **261**, 178–187.
23 C. Yu, J. Yang, C. T. Zhao, X. M. Fan, G. Wang and J. S. Qiu, *Nanoscale*, 2014, **6**, 3097–3104.
24 J. J. Zhou, Q. Li, C. Chen, Y. L. Li, K. Tao and L. Han, *Chem. Eng. J.*, 2018, **350**, 551–558.
25 X. Y. Li, G. P. Wan, J. Y. Xiao, L. H. Wu, S. H. Shi and G. Z. Wang, *Mater. Lett.*, 2018, **228**, 179–182.
26 P. Simon, Y. Gogotsi and B. Dunn, *Science*, 2014, **343**, 1210.
27 Y. Gogotsi and R. M. Penner, *ACS Nano*, 2018, **12**, 2081–2083.
28 T. Brousse, D. Bélanger and J. W. Long, *J. Electrochem. Soc.*, 2015, **162**, A5185–A5189.
29 M. R. Lukatskaya, B. Dunn and Y. Gogotsi, *Nat. Commun.*, 2016, **7**, 12647.
30 H. Maki, M. Takigawa and M. Mizuhata, *ACS Appl. Mater. Interfaces*, 2015, **7**, 17188–17198.
31 M. R. Lukatskaya, O. Mashtalir, C. E. Ren, Y. Dall'Agnese, P. Rozier, P. L. Taberna, M. Naguib, P. Simon, M. W. Barsoum and Y. Gogotsi, *Science*, 2013, **341**, 1502–1505.
32 M. Naguib, M. Kurtoglu, V. Presser, J. Lu, J. J. Niu, M. Heon, L. Hultman, Y. Gogotsi and M. W. Barsoum, *Adv. Mater.*, 2011, **23**, 4248–4253.
33 M. Naguib, J. Halim, J. Lu, K. M. Cook, L. Hultman, Y. Gogotsi and M. W. Barsoum, *J. Am. Chem. Soc.*, 2013, **135**, 15966–15969.

Published on 03 January 2019. Downloaded by University of Science and Technology of China on 5/29/2020 3:30:25 AM.

34 M. Ghidiu, M. R. Lukatskaya, M. Q. Zhao, Y. Gogotsi and M. W. Barsoum, *Nature*, 2014, **516**, 78–81.
35 B. Anasori, M. R. Lukatskaya and Y. Gogotsi, *Nat. Rev. Mater.*, 2017, **2**, 16098.
36 M. Naguib, O. Mashtalir, J. Carle, V. Presser, J. Lu, L. Hultman, Y. Gogotsi and M. W. Barsoum, *ACS Nano*, 2012, **6**, 1322–1331.
37 M. Naguib, V. N. Mochalin, M. W. Barsoum and Y. Gogotsi, *Adv. Mater.*, 2014, **26**, 992–1005.
38 Q. Tao, M. Dahlqvist, J. Lu, S. Kota, R. Meshkian, J. Halim, J. Palisaitis, L. Hultman, M. W. Barsoum, P. O. A. Persson and J. Rosen, *Nat. Commun.*, 2017, **8**, 14949.
39 Y. Wen, T. E. Rufford, X. Chen, N. Li, M. Lyu, L. Dai and L. Wang, *Nano Energy*, 2017, **38**, 368–376.
40 M. Yu, S. Zhou, Z. Wang, J. Zhao and J. Qiu, *Nano Energy*, 2018, **44**, 181–190.
41 M. H. Tran, T. Schäfer, A. Shahraei, M. Dürrschnabel, L. Molina-Luna, U. I. Kramm and C. S. Birkel, *ACS Appl. Energy Mater.*, 2018, **1**, 3908–3914.
42 M. Li, F. Liu, X. B. Zhang and J. P. Cheng, *Phys. Chem. Chem. Phys.*, 2016, **18**, 30068–30078.
43 R. Z. Ma, X. H. Liu, J. B. Liang, Y. Bando and T. Sasaki, *Adv. Mater.*, 2014, **26**, 4173–4178.
44 Z. J. Han, C. Huang, S. S. Meysami, D. Piche, D. H. Seo, S. Pineda, A. T. Murdock, P. S. Bruce, P. S. Grant and N. Grobert, *Carbon*, 2018, **126**, 305–312.
45 L. Shen, L. Yu, H. B. Wu, X. Y. Yu, X. Zhang and X. W. Lou, *Nat. Commun.*, 2015, **6**, 6694.
46 J. Y. Luo and Y. Y. Xia, *J. Power Sources*, 2009, **186**, 224–227.
47 N. F. Yu, L. J. Gao, S. H. Zhao and Z. D. Wang, *Electrochim. Acta*, 2009, **54**, 3835–3841.
48 X. L. Wu, L. L. Jiang, C. L. Long, T. Wei and Z. J. Fan, *Adv. Funct. Mater.*, 2015, **25**, 1648–1655.
49 H. Xia, C. Hong, B. Li, B. Zhao, Z. Lin, M. Zheng, S. V. Savilov and S. M. Aldoshin, *Adv. Funct. Mater.*, 2015, **25**, 627–635.
50 M. S. Kolathodi, M. Palei and T. S. Natarajan, *J. Mater. Chem. A*, 2015, **3**, 7513–7522.
51 X. Yu, B. Lu and Z. Xu, *Adv. Mater.*, 2014, **26**, 1044–1051.
52 S. Y. Kim, H. M. Jeong, J. H. Kwon, I. W. Ock, W. H. Suh, G. D. Stucky and J. K. Kang, *Energy Environ. Sci.*, 2014, **8**, 188–194.
53 Q. T. Qu, Y. Shi, S. Tian, Y. H. Chen, Y. P. Wu and R. Holze, *J. Power Sources*, 2009, **194**, 1222–1225.
54 C. Zhou, Y. Zhang, Y. Li and J. Liu, *Nano Lett.*, 2013, **13**, 2078–2085.
55 C. S. Dai, P. Y. Chien, J. Y. Lin, S. W. Chou, W. K. Wu, P. H. Li, K. Y. Wu and T. W. Lin, *ACS Appl. Mater. Interfaces*, 2013, **5**, 12168–12174.
56 C. Guan, X. M. Liu, W. N. Ren, X. Li, C. W. Cheng and J. Wang, *Adv. Energy Mater.*, 2017, **7**, 1602391.
57 X. Liu, N. Zhang, J. Ni and L. Gao, *J. Solid State Electrochem.*, 2013, **17**, 1939–1944.
58 F. X. Wang, X. W. Wu, X. H. Yuan, Z. C. Liu, Y. Zhang, L. J. Fu, Y. S. Zhu, Q. M. Zhou, Y. P. Wu and W. Huang, *Chem. Soc. Rev.*, 2017, **46**, 6816–6854.
59 J. Liu, J. Wang, C. Xu, H. Jiang, C. Li, L. Zhang, J. Lin and Z. X. Shen, *Adv. Sci.*, 2018, **5**, 1700322.
60 H. S. Kim, J. B. Cook, H. Lin, J. S. Ko, S. H. Tolbert, V. Ozolins and B. Dunn, *Nat. Mater.*, 2017, **16**, 454–460.
61 S. Niu, Z. Wang, M. Yu, M. Yu, L. Xiu, S. Wang, X. Wu and J. Qiu, *ACS Nano*, 2018, **12**, 3928–3937.

 This journal is © The Royal Society of Chemistry 2019